Energy Materials

Supplementary Material

Metal- and binder-free dual-ion battery based on green synthetic nano-embroidered spherical organic anode and pure ionic liquid electrolyte

Hongzheng Wu[1,2], Shenghao Luo[1,2], Wen Zheng[3], Li Li[3], Yaobing Fang[2,*], Wenhui Yuan[1,2,*]

[1]School of Chemistry and Chemical Engineering, South China University of Technology, Guangzhou 510640, Guangdong, China.
[2]Guangdong Engineering Technology Research Centre of Advanced Insulating Coating, South China University of Technology-Zhuhai Institute of Modern Industrial Innovation, Zhuhai 519175, Guangdong, China.
[3]School of Environment and Energy, South China University of Technology, Guangzhou 510640, Guangdong, China.

Correspondence to: Prof. Wenhui Yuan, School of Chemistry and Chemical Engineering, South China University of Technology, 381 Wushan Road, Tianhe District, Guangzhou 510640, Guangdong, China. E-mail: cewhyuan@scut.edu.cn

Calculation of specific energy density

Note the specific capacity of the anode is **qa** and that of the cathode is **qc**, the weight of anode is **ma** and that of cathode is **mc**, the total weight of electrolyte, collectors, and case is **MT**, and the total weight of the battery is **MD**. We take **qa** = 372 mAh g^{-1} and **qc** = 100 mAh g^{-1} here. The capacity of anode should be 10% higher than the capacity of cathode, namely, **ma*qa = 1.1*mc*qc**. Therefore, the mass ratio of anode and cathode in a dual-graphite battery is **ma = 0.3mc**.

Assume that the total mass of a coin-type battery is comprised of 60% from anode and cathode, and 40% from electrolyte, separator, collectors, and case. **ma + mc = 60%*MD**, So, **MB = 2.1 mc, MT = 0.84 mc**. In this battery system, as graphite paper acted as both cathode and current collector, the mc is 0. The weight ratio of anode (noted as **r**) should be **r = mc/(mc + MT) = 54%**. We note the specific energy density based on the weight of cathode as **Ec**, and that based on the weight of total battery as **ED**. Therefore, the

relationship between **Ec** and **ED** is **EB= 54%*Ec**, where **Ec** can be read directly from the charge-discharge test results.

Supplementary Table 1. The elemental percentages of C, N, and O according to the results of XPS-mapping.

Technology	o-PDI（%）			m-PDI（%）			p-PDI（%）		
	C	N	O	C	N	O	C	N	O
XPS-mapping	84.5	4.2	11.3	86.3	4.1	9.6	87.5	3.9	8.6

Supplementary Table 2. Comparison of the electrochemical performance of DIBs based on pure ionic liquid electrolytes.

Anode materials	Electrolytes	Capacity (mAh/g)	Retention	References
o-PDI	$Pyr_{14}TFSI$	144 at 0.2 C	100% after 4000 cycles at 10 C	This work
m-PDI	$Pyr_{14}TFSI$	222 at 0.2 C	100% after 4000 cycles at 10 C	This work
p-PDI	$Pyr_{14}TFSI$	168 at 0.2 C	100% after 4000 cycles at 10 C	This work
NTCDA	EMImTFSI	114 at 0.1 C	71.38% after 100 cycles at 2 C	1
Graphite	$Pyr_{14}TFSI$	49 at 0.5 C	60% after 100 cycles at 0.5 C	2
MoS_2	EMImTFSI	77 at 0.5 C	84.3% after 300 cycles at 4 C	3
KS6	EMImTfO	46.2 at 4 C	71% after 100 cycles at 4 C	4
CG	$PP_{14}TFSI$	82 at 0.3 C	100% after 600 cycles at 3 C	5

PAQS	$Pyr_{13}TFSI$	47.4 at 2 C	91.4% after 100 cycles at 2 C	6
PAQS	$PP_{14}TFSI$	43 at 1 C	98.3% after 100 cycles at 1 C	7
Graphene	$EMImPF_6$	/	90% after 1000 cycles	8
AC	$EMImPF_6$	/	83% after 50 cycles at 5 C	9
PAQS	$Pyr_{14}TFSI$	101 at 10 C	84.9% after 1000 cycles at 120 C	10
Graphite	$DMPIAlCl_4$	80 at 3 C	92% after 500 cycles at 3 C	11
PCT	$Pyr_{14}TFSI$	164.5 at 0.1 C	92.2% after 100 cycles at 5 C	12
PI/NaCl	EMImTFSI	79 at 1 C	96% after 300 cycles at 5 C	13
GP	$PP_{14}NTF_2$	56.9 at 2 C	74.7% after 100 cycles at 2 C	14
SP	$DMPIAlCl_4$	77 at 3 C	92% after 300 cycles at 3 C	15

Supplementary Table 3. Comparison of the self-discharge rate with other reported DIBs.

DIBs Structure	Self-discharge rate	Current density	Reference
o-PDI (-) // $Pyr_{14}TFSI$ // Graphite paper (+)	0.817% h^{-1}	300 mA g^{-1}	This work
m-PDI (-) // $Pyr_{14}TFSI$ // Graphite paper (+)	0.371% h^{-1}	300 mA g^{-1}	This work
p-PDI (-) // $Pyr_{14}TFSI$ // Graphite paper (+)	0.603% h^{-1}	300 mA g^{-1}	This work
α-Fe_2O_3 (-) // LiTFSI-$Pyr_{14}TFSI$ // Graphite (+)	1.1% h^{-1}	200 mA g^{-1}	16
Graphite (-) //$AlCl_3$-EMImCl // Graphite (+)	16.82% h^{-1}	500 mA g^{-1}	17
PCT (-) // $Pyr_{14}TFSI$ // Graphite (+)	4.68% h^{-1}	100 mA g^{-1}	12
MoS_2 (-) // EMImTFSI // Graphite (+)	16.5% h^{-1}	400 mA g^{-1}	3
Graphite (-) // $PP_{14}TFSI$ // Graphite (+)	12% h^{-1}	0.65 mA cm^{-2}	5
Active carbon (-) // Li_2SO_4 // Active carbon (+)	2% h^{-1}	/	18
NTCDA (-) // $Pyr_{14}TFSI$ // Natural graphite (+)	6.12% h^{-1}	10 mA g^{-1}	1

PPTO@CNTs (-) // $NaPF_6$-DEGDME // Na (+)	4.58% h^{-1}	100 mA g^{-1}	19
3D-NTC750(-) // KPF_6-EC-DEC // PTCDA (+)	0.088% h^{-1}	200 mA g^{-1}	20
Blending graphite (-) // $LiPF_6$-FEC-FEMC // Blending graphite (+)	1.56% h^{-1}	100 mA g^{-1}	21
Li (-) // $LiPF_6$-EMC // NG@PPA (+)	0.55% h^{-1}	100 mA g^{-1}	22

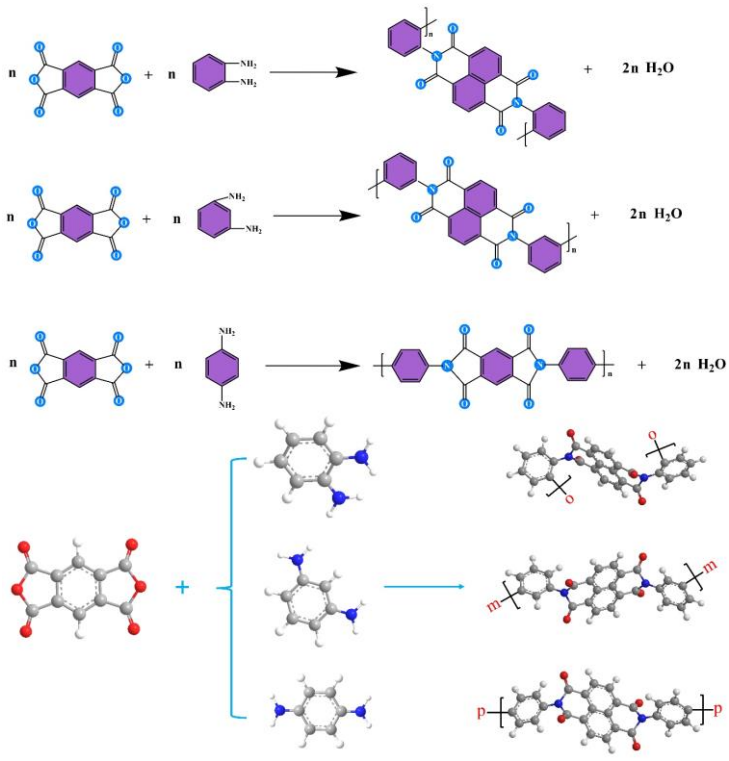

Schematic S1. Schematic diagram of the synthesis reaction of o-PDI, m-PDI, and p-PDI.

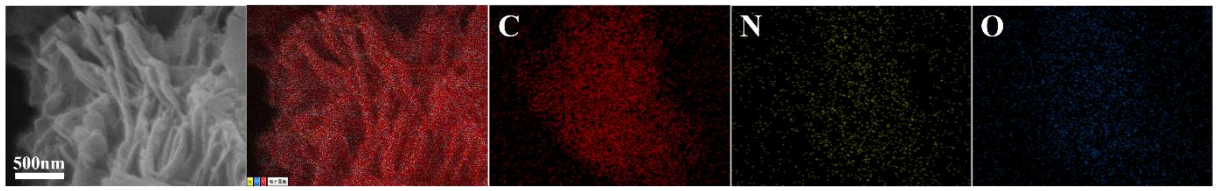

Supplementary Figure S1. Highly directed SEM of o-PDI and corresponding EDS mapping.

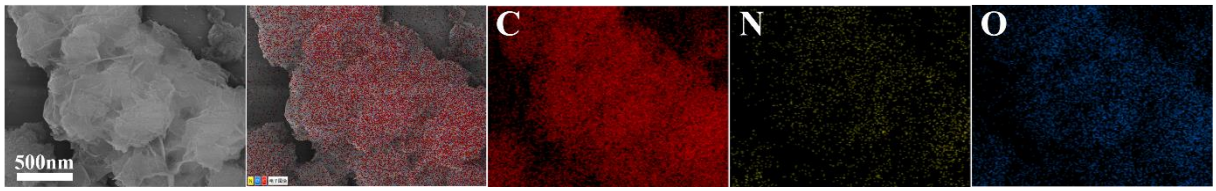

Supplementary Figure S2. Highly directed SEM of p-PDI and corresponding EDS mapping.

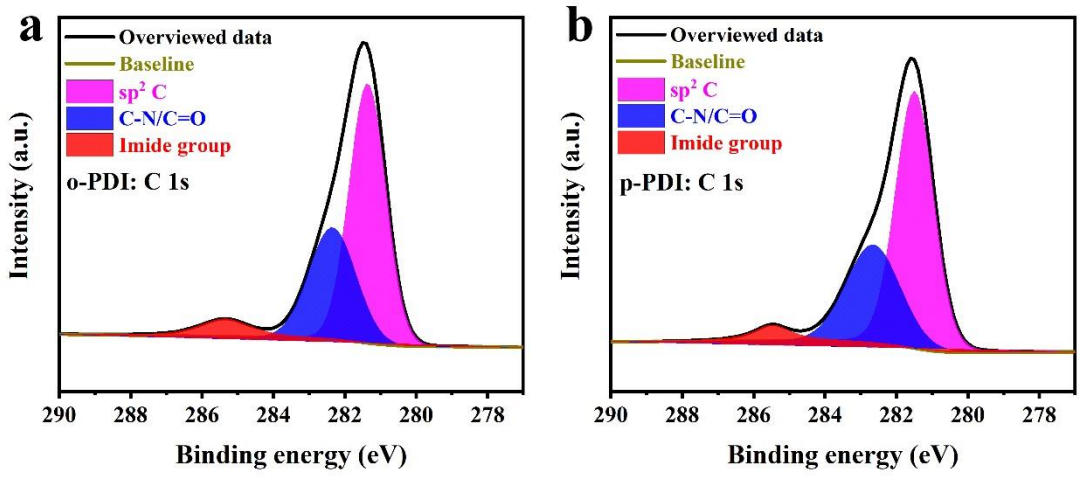

Supplementary Figure S3. XPS high-resolution C 1s fitted spectra of (a) o-PDI and (b) p-PDI.

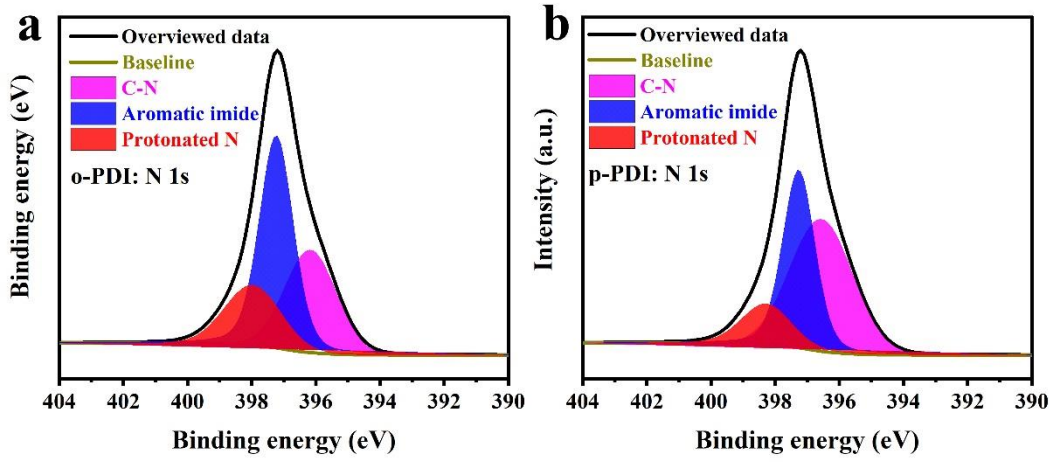

Supplementary Figure S4. XPS high-resolution N 1s fitted spectra of (a) o-PDI and (b) p-PDI.

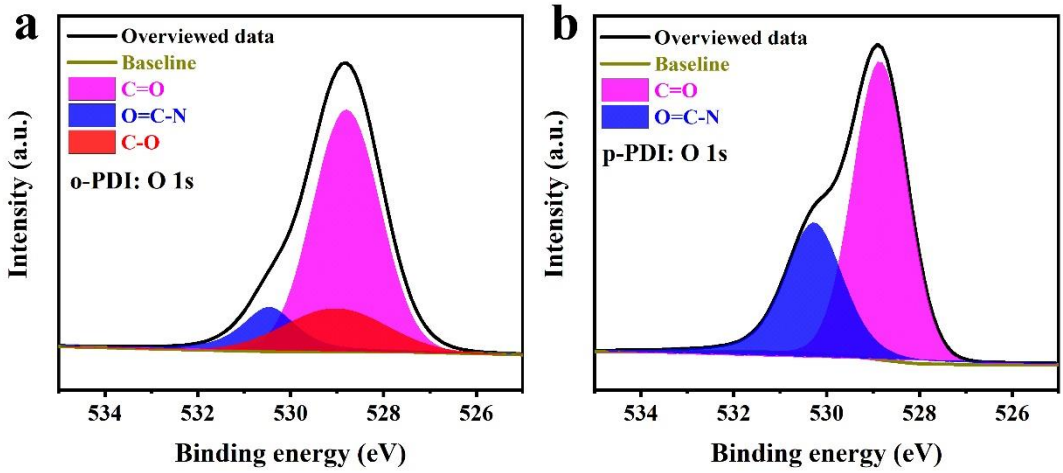

Supplementary Figure S5. XPS high-resolution O 1s fitted spectra of (a) o-PDI and (b) p-PDI.

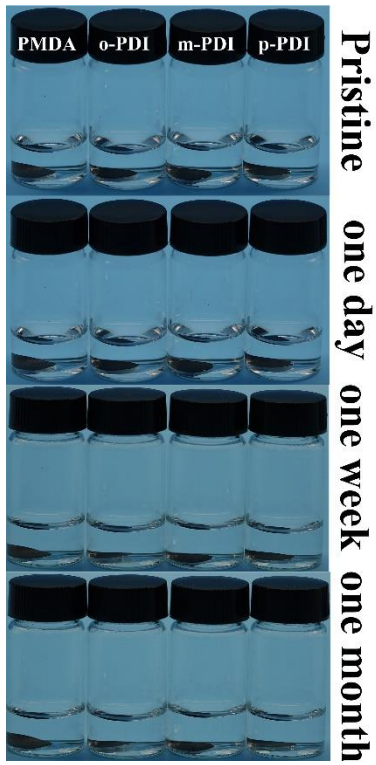

Supplementary Figure S6. Digital photos of color variation based on $Pyr_{14}TFSI$ ionic liquid system.

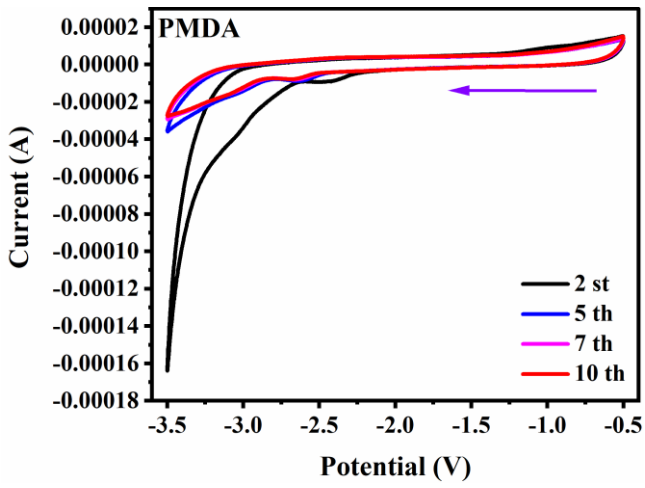

Supplementary Figure S7. CV curves of PMDA electrode at 1 mV/s with different cycles.

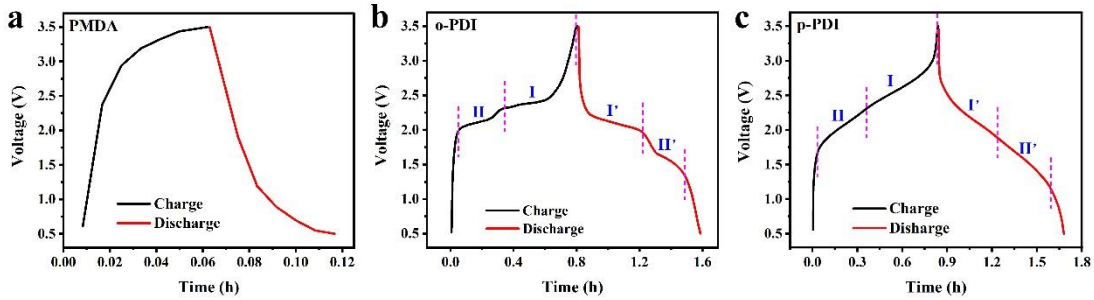

Supplementary Figure S8. The GCD curves of (a) PMDA, (b) o-PDI and (c) m-PDI.

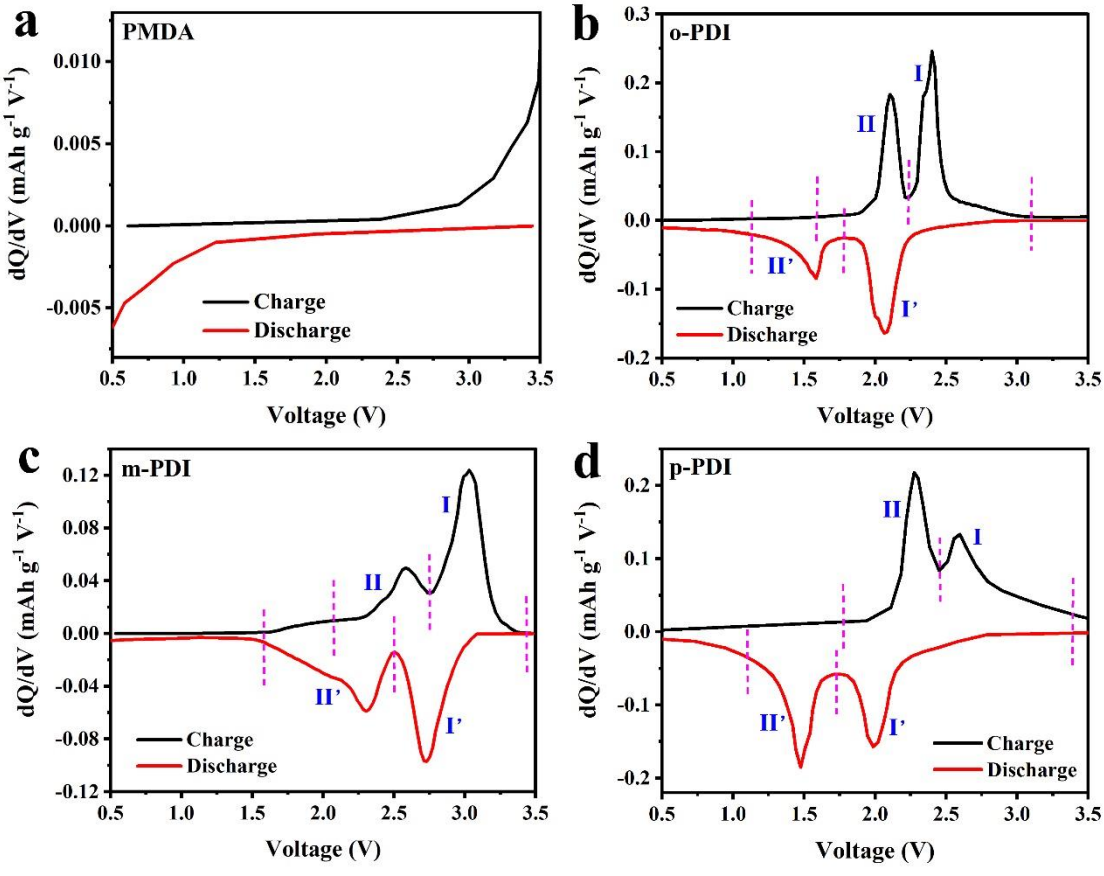

Supplementary Figure S9. The dQ/dV curves of (a) PMDA, (b) o-PDI and (c) m-PDI.

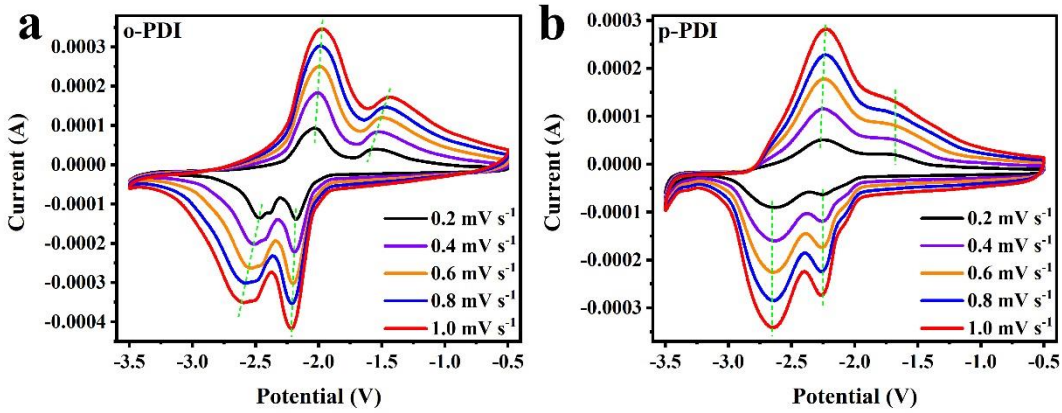

Supplementary Figure S10. CV curves at different scan rates for (a) o-PDI and (b) p-PDI.

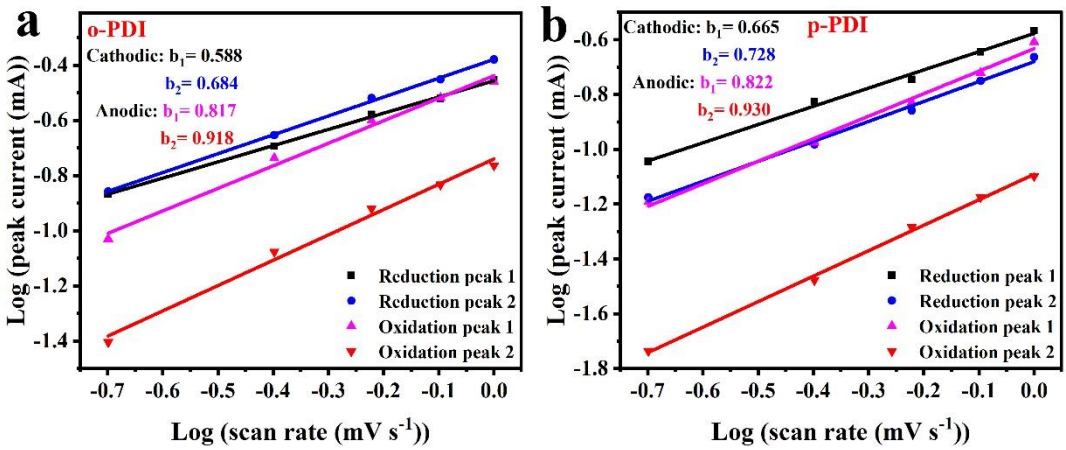

Supplementary Figure S11. b-values of (a) o-PDI and (b) p-PDI based on redox peaks.

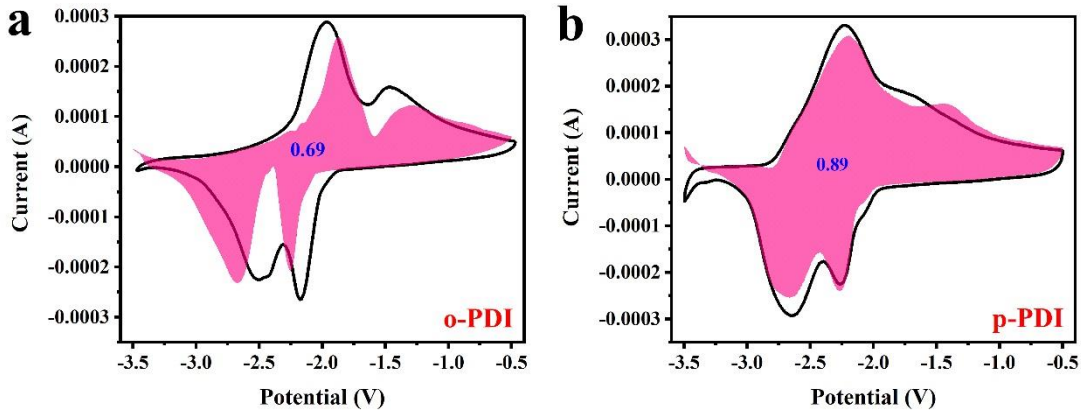

Supplementary Figure S12. Pseudocapacitance contribution of (a) o-PDI and (b) p-PDI at 1 mV/s.

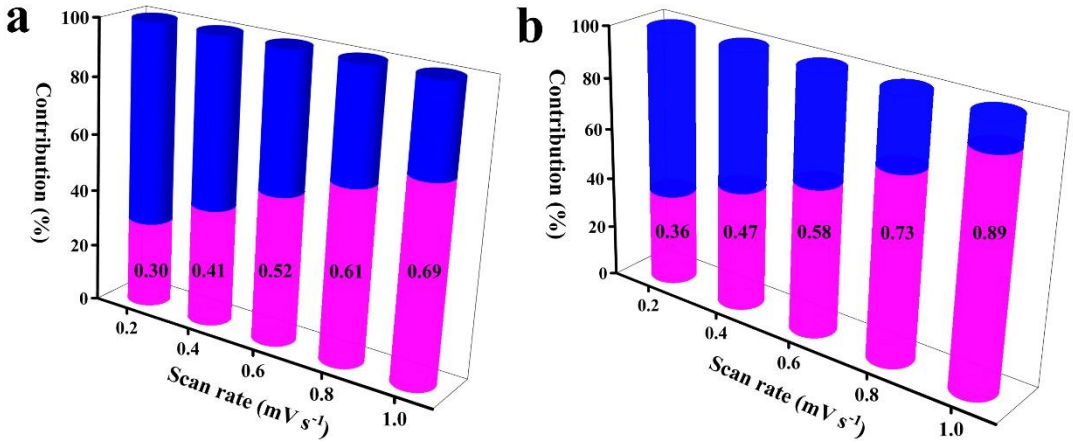

Supplementary Figure S13. Pseudocapacitance contribution of (a) o-PDI and (b) p-PDI at different rates.

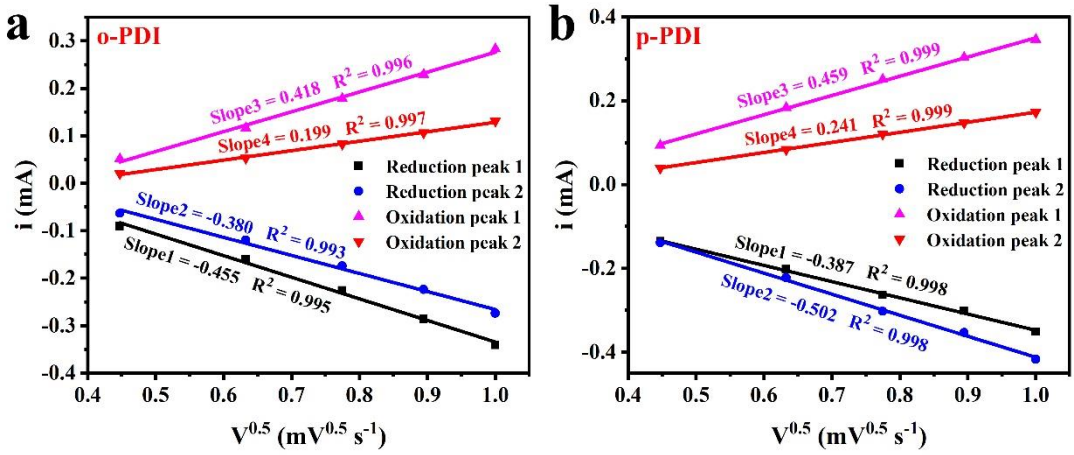

Supplementary Figure S14. Linear relationship between the peak current and the square root of scan rates under redox peaks. (a) o-PDI and (b) p-PDI.

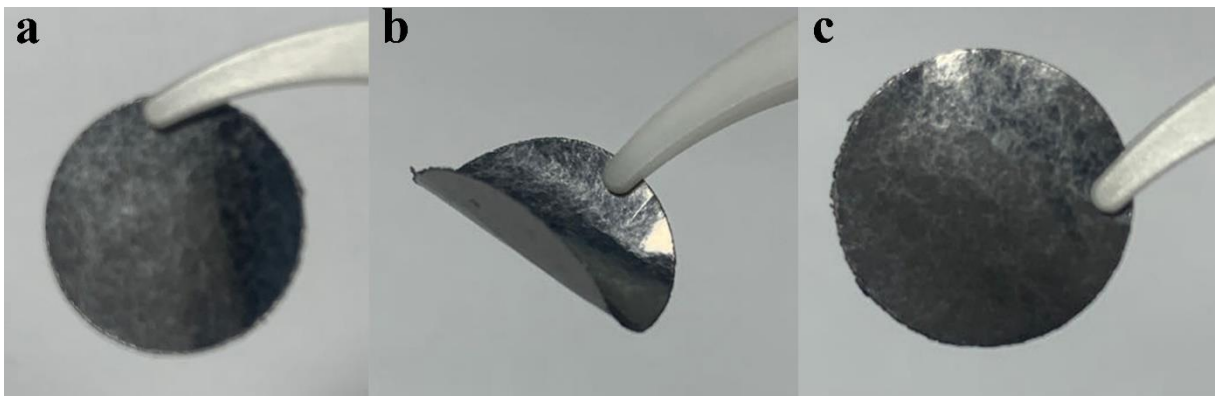

Supplementary Figure S15. Graphite paper before (a) bending, (b) after bending and (c) after spreading.

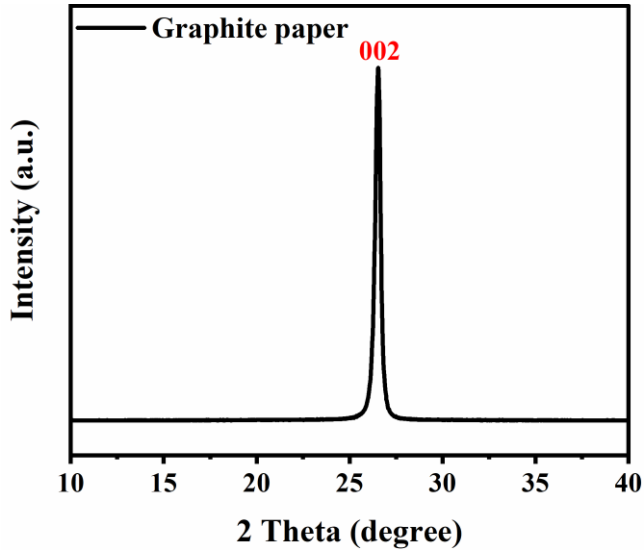

Supplementary Figure S16. XRD characterization of graphite paper.

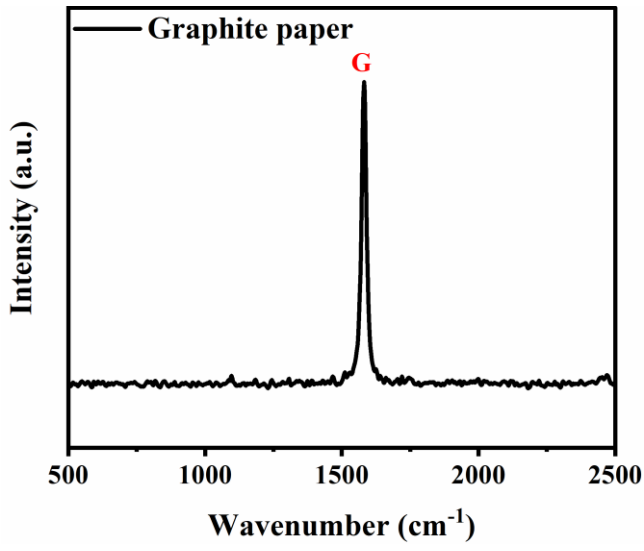

Supplementary Figure S17. Raman characterization of graphite paper.

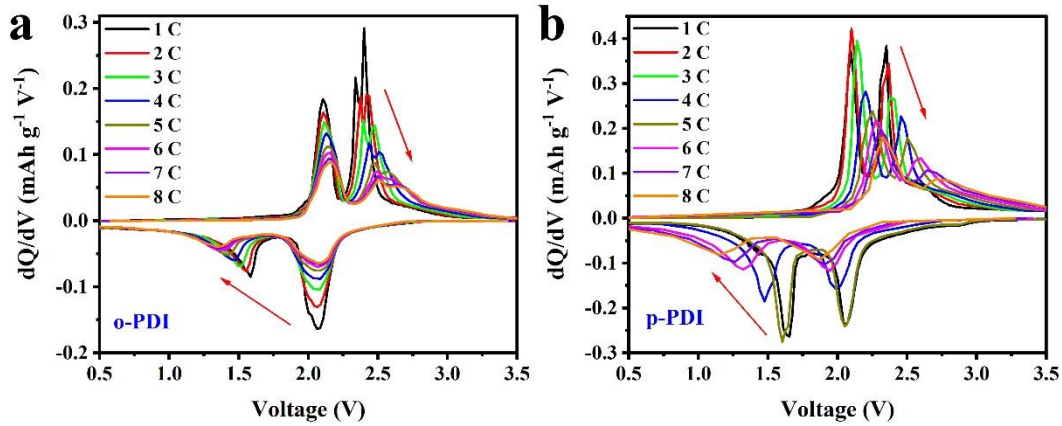

Supplementary Figure S18. dQ/dV curves of (a) o//G-DIB and (b) p//G-DIB at different rates.

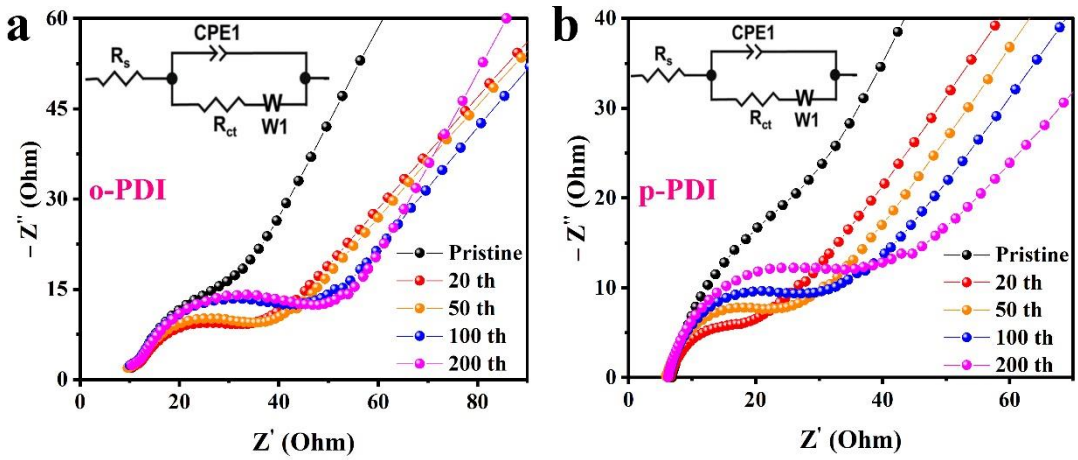

Supplementary Figure S19. Electrochemical impedance spectra of (a) o//G-DI and (b) p//G-DIB.

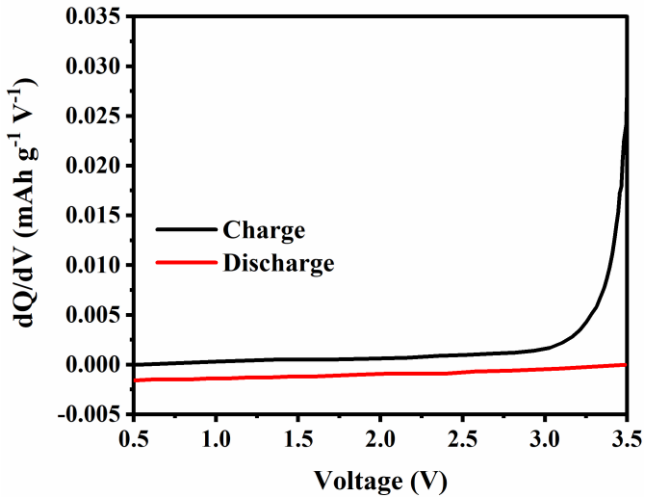

Supplementary Figure S20. The dQ/dV curve of conductive agent Super P.

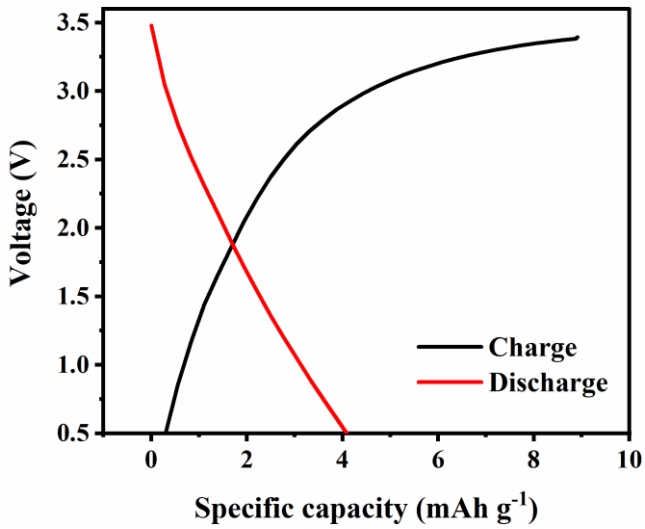

Supplementary Figure S21. The GCD curve of conductive agent Super P.

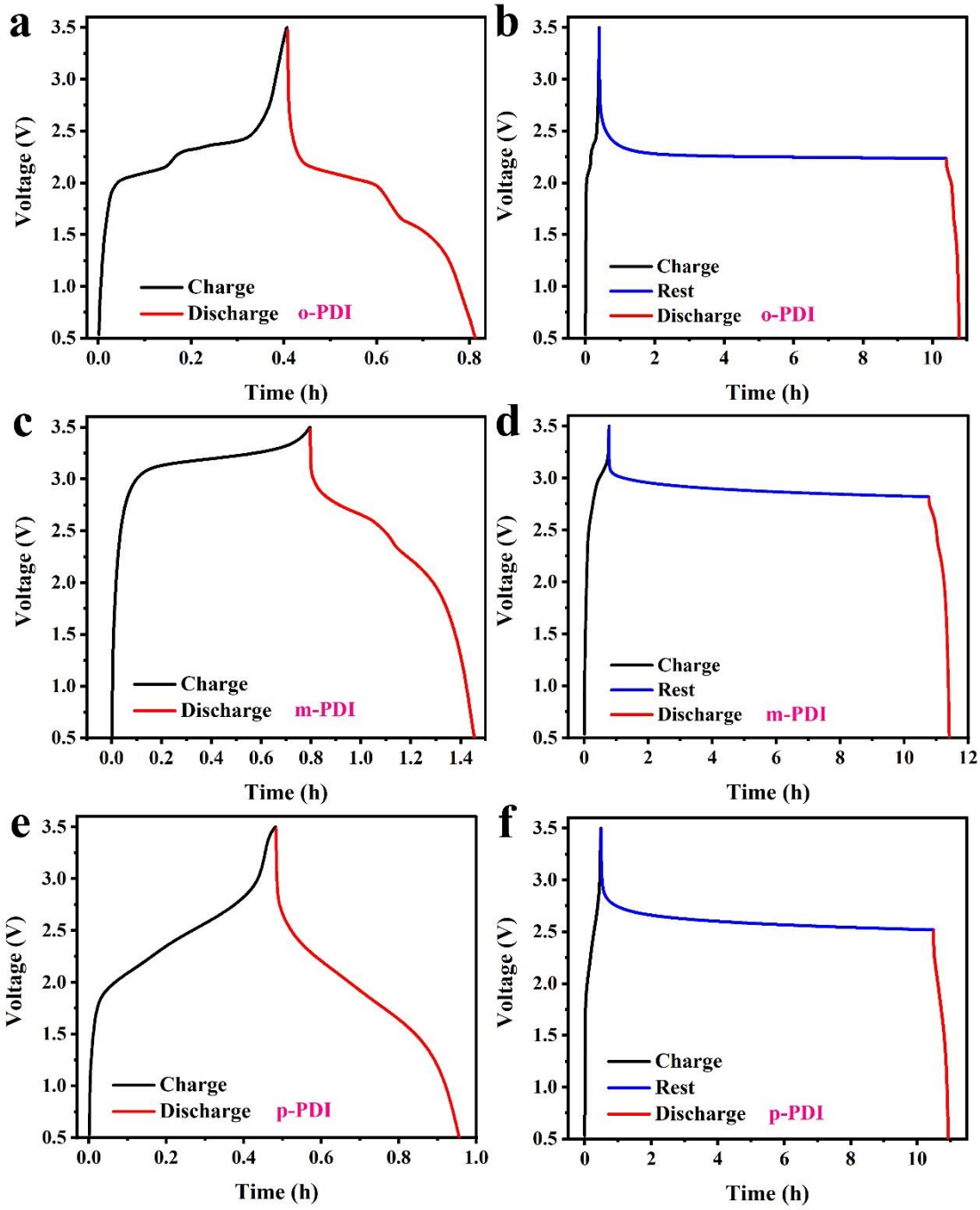

Supplementary Figure S22. The resting and unresting time-voltage curves of (a-b) o//G-DIB, (c-d) m//G-DIB and (e-f) p//G-DIB.

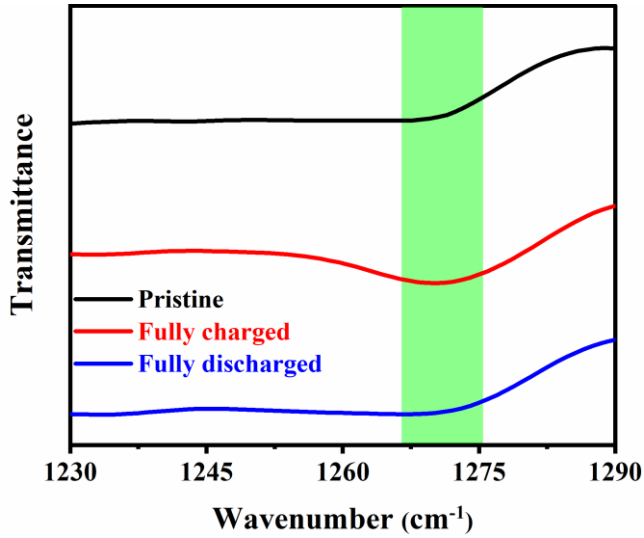

Supplementary Figure S23. FT-IR characterization of m//G-DIB under pristine, fully charged and fully discharged states.

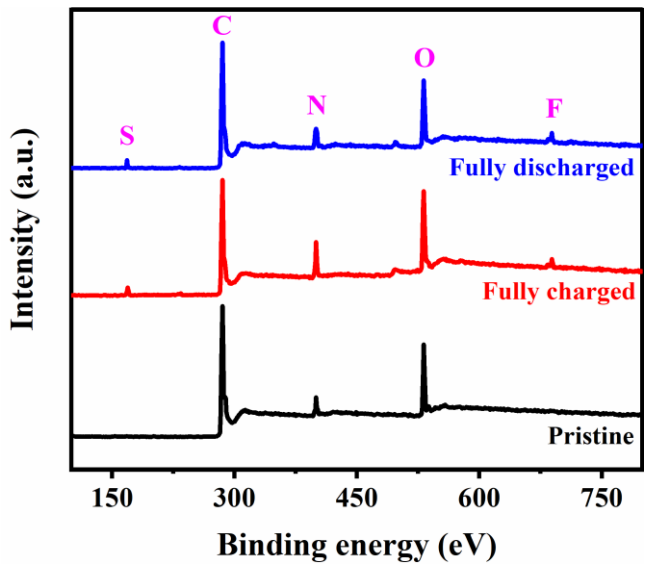

Supplementary Figure S24. XPS characterizations of anode under pristine, fully charged/discharged state.

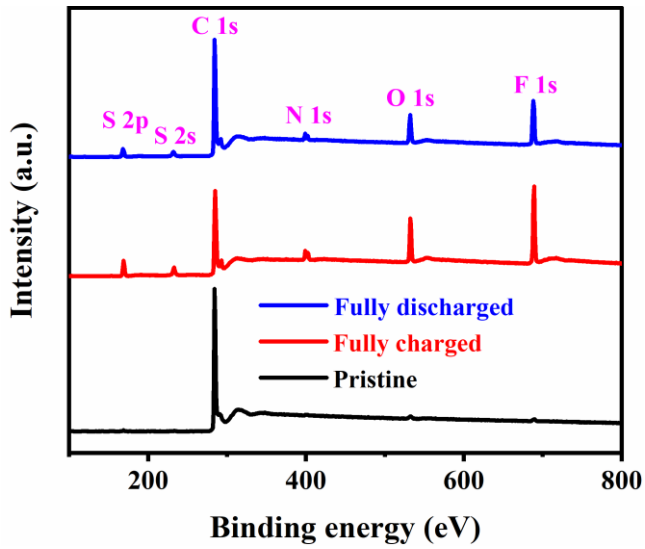

Supplementary Figure S25. XPS full spectra of m//G-DIB under pristine, fully charged and fully discharged states.

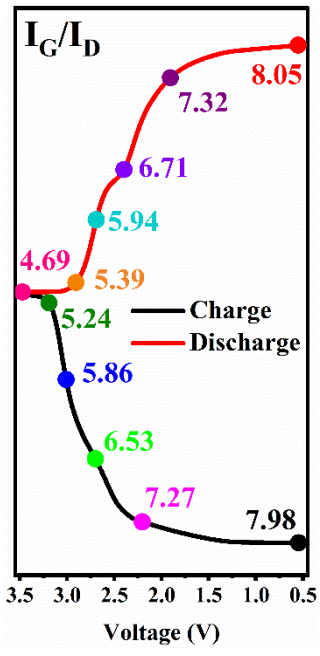

Supplementary Figure S26. The I_G/I_D values based on different charging and discharging stages.

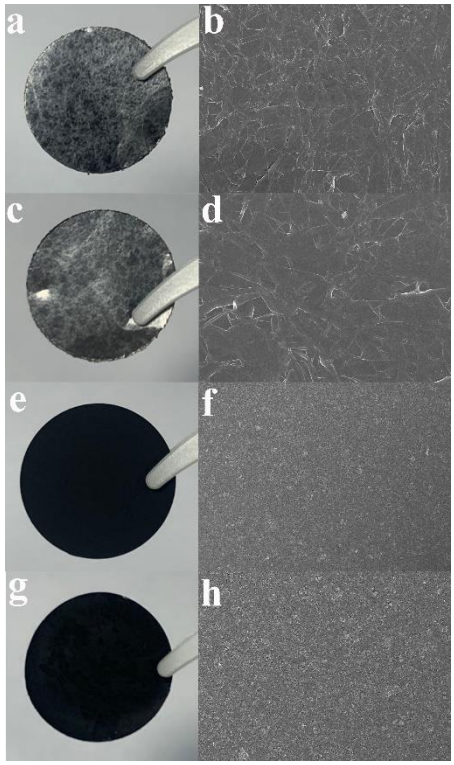

Supplementary Figure S27. The morphology of the origin and after 1000 cycles: (a-b) Cathode before cycling, (c-d) Cathode after 1000 cycles, (e-f) Anode before cycling, (g-h) Anode after 1000 cycles.

REFERENCES

1. W. C. Zhu, Y. Huang, B. Jiang, R. G. Xiao. A metal-free ionic liquid dual-ion battery based on the reversible interaction of 1-butyl-1-methylpyrrolidinium cations with 1,4,5,8-naphthalenetetracarboxylic dianhydride. J Mol Liq. **339**((2021). 116789 https://doi.org/ARTN10.1016/j.molliq.2021.116789

2. A. Y. Wang, W. H. Yuan, J. X. Fan, L. Li. A dual-graphite battery with pure 1-butyl-1-methylpyrrolidinium bis(trifluoromethylsulfonyl) imide as the electrolyte. Energy Technol-Ger. **6**(11), 2172-2178 (2018). https://doi.org/10.1002/ente.201800269

3. J. X. Fan, Q. Q. Xiao, Y. B. Fang, L. Li, W. Y. Feng, W. H. Yuan. Reversible

intercalation of 1-ethyl-3-methylimidazolium cations into mos_2 from a pure ionic liquid electrolyte for dual-ion cells. Chemelectrochem. **6**(3), 676-683 (2019). https://doi.org/10.1002/celc.201801583

4. Y. Huang, R. G. Xiao, Z. M. Ma, W. C. Zhu. Developing dual-graphite batteries with pure 1-ethyl-3-methylimidazolium trifluoromethanesulfonate ionic liquid as the electrolyte. Chemelectrochem. **6**(17), 4681-4688 (2019). https://doi.org/10.1002/celc.201901171

5. J. X. Fan, Z. X. Zhang, Y. H. Liu, A. Y. Wang, L. Li, W. H. Yuan. An excellent rechargeable $pp_{14}tfsi$ ionic liquid dual-ion battery. Chem Commun. **53**(51), 6891-6894 (2017). https://doi.org/10.1039/c7cc02534c

6. H. Liu, W. C. Zhu, H. Y. Zhou, J. Z. Wang. Research of dual-ion polymer batteries based on -butyl-methylpiperidinium bis(trifluoromethylsulfonyl)imide ionic liquid electrolyte. Ionics. **28**(9), 4103-4110 (2022). https://doi.org/10.1007/s11581-022-04652-x

7. X. Y. Shi, T. Deng, B. S. Zhang, W. Zhang, L. Sui, H. Yang, D. Wang, W. Shi, C. M. Chen, W. T. Zheng. Accessible 3d integrative paper electrode shapes: All-carbon dual-ion batteries with optimum packaging performances. Chemelectrochem. **4**(12), 3238-3243 (2017). https://doi.org/10.1002/celc.201700752

8. H. Yang, X. Y. Shi, T. Deng, T. T. Qin, L. Sui, M. Feng, H. Chen, W. Zhang, W. T. Zheng. Carbon-based dual-ion battery with enhanced capacity and cycling stability. Chemelectrochem. **5**(23), 3612-3618 (2018). https://doi.org/10.1002/celc.201801108

9. Y. B. Fang, W. Zheng, L. Li, W. H. Yuan. An ultrahigh rate ionic liquid dual-ion battery

based on a poly(anthraquinonyl sulfide) anode. Acs Applied Energy Materials. **3**(12), 12276-12283 (2020). https://doi.org/10.1021/acsaem.0c02335

10. K. Y. Lin, T. L. Hsieh, Y. H. Wu, M. C. Lin. Sustainable recycling of spent ionic liquid dual-ion batteries. Energy Technol-Ger. **11**(1), (2023). https://doi.org/10.1002/ente.202200938

11. Y. B. Fang, C. Y. Chen, J. X. Fan, M. D. Zhang, W. H. Yuan, L. Li. Reversible interaction of 1-butyl-1-methylpyrrolidinium cations with 5,7,12,14-pentacenetetrone from a pure ionic liquid electrolyte for dual-ion batteries. Chem Commun. **55**(57), 8333-8336 (2019). https://doi.org/10.1039/c9cc04626g

12. R. J. Shi, L. J. Liu, Y. Lu, Y. X. Li, S. B. Zheng, Z. H. Yan, K. Zhang, J. Chen. In situ polymerized conjugated poly(pyrene-4,5,9,10-tetraone)/carbon nanotubes composites for high-performance cathode of sodium batteries. Advanced Energy Materials. **11**(6), (2021). 2002917 https://doi.org/ARTN10.1002/aenm.202002917

13. Z. C. Lv, M. Han, J. H. Sun, L. X. Hou, H. Chen, Y. X. Li, M. C. Lin. A high discharge voltage dual-ion rechargeable battery using pure (dmpi) (alcl) ionic liquid electrolyte. Journal of Power Sources. **418**(233-240 (2019). https://doi.org/10.1016/j.jpowsour.2019.02.035

14. H. Z. Wu, L. Li, W. H. Yuan. Nano-cubic α-fe_2o_3 anode for li/na based dual-ion full battery. Chemical Engineering Journal. **442**((2022). https://doi.org/ARTN 136259 10.1016/j.cej.2022.136259

15. Z. Y. Li, J. Liu, B. B. Niu, J. L. Li, F. Y. Kang. A novel graphite-graphite dual ion battery using an alcl-[emim]cl liquid electrolyte. Small. **14**(28), (2018). 1800745

https://doi.org/ARTN10.1002/smll.201800745

16. L. García-Cruz, P. Ratajczak, J. Iniesta, V. Montiel, F. Béguin. Self-discharge of ac/ac electrochemical capacitors in salt aqueous electrolyte. Electrochimica Acta. **202**(66-72 (2016). https://doi.org/10.1016/j.electacta.2016.03.159

17. W. L. Zhang, J. Yin, M. L. Sun, W. X. Wang, C. L. Chen, M. Altunkaya, A. H. Emwas, Y. Han, U. Schwingenschlögl, H. N. Alshareef. Direct pyrolysis of supermolecules: An ultrahigh edge-nitrogen doping strategy of carbon anodes for potassium-ion batteries. Advanced Materials. **32**(25), (2020). https://doi.org/ARTN 200073210.1002/adma.202000732

18. Y. Wang, Y. J. Zhang, S. Y. Dong, W. C. Zhou, P. K. Lee, Z. H. Peng, C. Q. Dang, P. H. L. Sit, J. P. Guo, D. Y. W. Yu. An all-fluorinated electrolyte toward high voltage and long cycle performance dual-ion batteries. Advanced Energy Materials. **12**(19), (2022). 2103360 https://doi.org/ARTN10.1002/aenm.202103360

19. K. J. Zhang, D. C. Li, J. Shao, Y. Jiang, L. Z. Lv, Q. Shi, Q. T. Qu, H. H. Zheng. Ultrafast charge and long life of high-voltage cathodes for dual-ion batteries via a bifunctional interphase nanolayer on graphite particles. Small. **19**(12), (2023). https://doi.org/10.1002/smll.202206360

20. B. Jiang, T. Y. Kong, Z. H. Cai, W. C. Zhu, R. G. Xiao. In-situ modification of polyimide anode materials in dual-ion batteries. Electrochimica Acta. **435**((2022). 141402 https://doi.org/ARTN10.1016/j.electacta.2022.141402

21. W. C. Zhu, R. G. Xiao, Z. H. Cai, Y. Huang, J. B. Chen. Electrochemically active layer on the surface of poly(anthraquinonyl sulfide) anode in dual-ion batteries. Polymer.

212((2021). 123167 https://doi.org/ARTN10.1016/j.polymer.2020.123167

22. Z. Y. Li, J. Liu, J. L. Li, F. Y. Kang, F. Gao. A novel graphite-based dual ion battery using pp14ntf2 ionic liquid for preparing graphene structure. Carbon. **138**(52-60 (2018). https://doi.org/10.1016/j.carbon.2018.06.002